Chapter 8 – NUMERICAL SOLUTIONS FOR THE CAWAPI CONFIGURATION ON UNSTRUCTURED GRIDS AT EADS-MAS, GERMANY

by

Willy Fritz

This chapter presents some essential results which were obtained within the Cranked Arrow Wing Aerodynamics Project International (CAWAPI). In the CAWAPI, flight test data of the F-16XL aircraft were exploited as test cases for the verification and validation of CFD codes. The chapter focuses on the use of solution adapted hybrid grids with the DLR TAU code. Results for four different flight conditions (FC) will be presented and discussed. Comparisons with flight test data are shown for surface pressure distributions, boundary layer data and surface skin friction coefficients. The results show, that also for a complex configuration, solution adapted grids can fix the grid dependency of the numerical solution.

8.1 NOMENCLATURE

FT	=	flight test
tpl	=	total pressure loss
v/v_e	=	ratio of velocity magnitude in boundary layer to that at the rake extreme total-pressure tube
x/c_{local}	=	fractional distance along the local chord, positive aft
$2y/b_{local}$	=	fractional distance along the local semi span, positive towards the right wing tip
y+	=	dimensionless sublayer scale, $u_\tau y/\nu$

8.2 INTRODUCTION

The evolution of Computational Fluid Dynamics (CFD) and the rapidly increasing computational resources have enabled the aeronautical industry to simulate the aerodynamic behavior of realistic configurations. Nowadays this simulation is no longer limited to the computation of steady aerodynamic control characteristics, but also high-fidelity coupled multidisciplinary applications like the simulation of maneuvering fighter aircraft [8-1], [8-2] are possible. With the unstructured approach, the complexity of the geometry is also no longer a severe limitation. Within these coupled multidisciplinary applications (unsteady aerodynamics/flight mechanics/ aeroelastics coupling) the accuracy of the computed aerodynamic characteristics is very often the vital factor for the success of the simulation. So even at times of multidisciplinary applications validation of CFD codes with respect to accuracy and efficiency is still an important theme.

Typical validation data are obtained by wind tunnel measurements on generic configurations. Such data are commonly open to the community, but they are influenced by scaling effects, Re-number effects, and wind-tunnel blockage effects.

The validation of CFD for vortical flows was the purpose for the establishment of the RTO AVT-113 working group. One facet of this working group was the “Cranked Arrow Wing Aerodynamics Project International”

(CAWAPI). This project was started by NASA to allow a comprehensive comparison of several CFD codes with the flight test database of the F-16XL aircraft [8-3]. A more detailed overview on the CAWAPI is given by Lamar et al in Ref. [8-4].

The F-16XL flight test data base includes surface pressure measurements, boundary layer rakes data, and hot film data. This experimental data and the detailed geometry definition were provided by NASA for the use within the CAWAPI. Many of the flight conditions have vortical flow conditions and are thus representative for high performance fighter aircraft.

By this, CAWAPI was an excellent opportunity for EADS-MAS to test the CFD tools with respect to accuracy and computational effort on a realistic configuration at realistic flow conditions. Validation could be done not only by comparison with flight test data, but also by comparison of numerical results obtained by different codes. The main interest of EADS-MAS in this project was however not only to produce a flow solution in a certain grid, but also to get experience and guidelines for the handling of complex configurations with respect to grid generation. In order to realize this by grid refinement and finally by solution based grid adaptation, EADS-MAS had to generate own hybrid grids and did not use any common grid.

The chapter reports on the numerical simulations contributed by EADS-MAS to the CAWAPI and concentrates on the four flight conditions ("FCs") FC 7 ($M_\infty = 0.304$, $\alpha = 12°$, Re = 44.4 x 10^6), FC 19 ($M_\infty = 0.36$, $\alpha = 12°$, Re = 46.8 x 10^6), FC 25 ($M_\infty = 0.25$, $\alpha = 19.84°$, Re = 32.22 x 10^6) and FC 70 ($M_\infty = 0.97$, $\alpha = 4.37°$, Re = 88.77 x 10^6). It shows in detail the effect of the grid adaptation on the numerical solution by a comparison of results obtained in different hybrid grids.

8.3 GEOMETRY

The geometry used in the CAWAPI project was the F-16XL aircraft. It was obtained from the Full-Scale F-16A aircraft by stretching the fuselage and adding a cranked-arrow wing. The wing has a leading edge sweep of 70° inboard and 50° outboard of this crank. At the wing apex, an "S-blend curve" is used to join the wing leading edge to the fuselage. Some essential details of the geometry are the airdam (upper surface fence mounted near the wing leading edge crank) and the tip missile with its rail. Both details were present during the test flights. A detailed description of the aircraft geometry is given in Refs. [8-3], [8-4] and in Chapters 3 and 4. The aircraft geometry was available as an IGES file, which was generated by Lockheed-Martin Aeronautics Company. In this geometry definition file the inlet up to the compressor face and the nozzle up to the turbine face were included but all control surfaces were not deflected. More details about the generation of the IGES file and other geometry preparing can be seen in [8-5] and Chapter 4. The file still contained multiple overlaying surfaces, which have been corrected at EADS-M, where a single set of describing surfaces was generated. Furthermore the gap between the Nozzle and the wing trailing edge flap was closed. All other geometric details (airdam, gap between launcher and missile, step at rear end wing fuselage junction) were kept for the grid generation. Finally the dimension of the geometry has been transferred from inches into meters. Figure 8-1 shows the resulting surface geometry as it was used for the grid generation. (The figure shows a solid model of the final surface grid which was used for the CFD simulations).

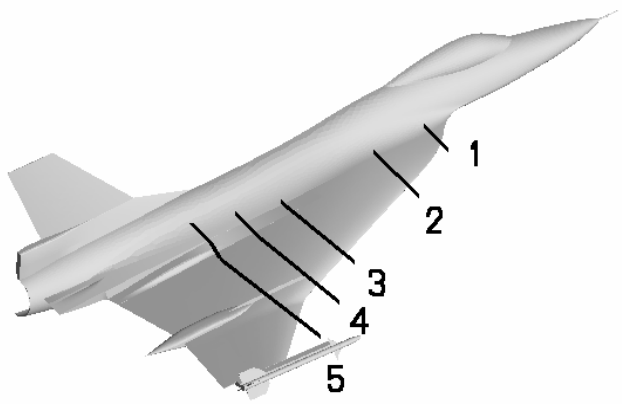

Figure 8-1: Surface Geometry of the F-16XL Aircraft Used in the CFD-Simulations.

A further interesting detail of the geometry is the shape of the leading edge. At the apex (position 1 in Figure 8-1), the wing starts with a kind of cropped sharp leading edge, which merges towards a round leading edge (position 2). At position 3 there is again a transition towards a sharp leading edge and the outer part of the wing finally has a sharp leading edge.

8.4 TEST CASES

Seven different test cases (Flight Conditions, FC) have been selected from the flight test database ([8-3], [8-4]) for the use in the RTO/AVT-113 task group. The present chapter will show results for four of those test cases, which have also been calculated by all the other members of the task group (Refs. [8-10]-[8-18] and Chapters 5 through 15). They are shown in Table 8-1.

Table 8-1: Calculated Flight Conditions

Flight Condition	Actual Mach Number	Actual Alpha (degrees)	Actual Beta (degrees)	Actual Reynolds Number
FC 7	0.304	11.89	-0.133	44.4E+06
FC 19	0.36	11.85	+0.612	44.8E+06
FC 25	0.242	19.84	+0.725	32.22E+06
FC 70	0.97	4.37	+0.310	88.77E+06

For all the above flight conditions a sideslip angle of 0 degrees was assumed thus they were calculated as symmetric. FC 7 was chosen, as boundary layer data (velocity profiles) from flight test were available and for FC 19 there exist surface skin friction data. Flight Condition 25 is that with the highest angle of attack. These 3 FCs all should have a vortical flow field. Finally FC 70 is a transonic test case with a very low angle of attack. For FC 7, FC 25, and FC 70 the calculations were started with a common initial grid and then continued with 4 individual solution based grid adaptation steps for each flight condition. As the conditions for FC 7 and FC 19 were very close, the final adapted grid of FC 7 was also used for FC 19. Each of the four flight conditions was also calculated in the so called “manually adapted” grid of Figure 8-4.

8.5 GRID GENERATION

8.5.1 General Remarks

As it was not sure whether a common unstructured grid could be used by all participants (specific requirements of the different flow solvers) and as also a systematic grid refinement study was planned, EADS-MAS decided to generate an own hybrid grid right from the start. For this the commercial hybrid grid generator from "CentaurSoft" was used [8-6]. This grid generation tool is based on the advancing front method and enables the generation of hybrid grids with minimal user interaction. Starting from the "air-tight" geometry, the grid generation process is split up into surface triangulation, prismatic grid generation and tetrahedral grid generation. Point clustering is achieved by automatic clustering based on geometric features and by user-controlled clustering, placing so called sources. This user controlled clustering has been used for a rough adaptation of the grid to the expected vortical flow structure. The surface triangulation works patch-oriented, which results in a not always needed high resolution of all small surface patches. (The geometry definition of the F-16XL aircraft contains several such mini-patches).

First flow calculations with such "manually adapted" grids were however not very satisfactory. Especially for the test cases with vortical flow structure the leeward suction peaks due to the leading edge vortices were under predicted and even grids with up to 22 million grid points were no guarantor for proper flow solutions. So it was clear, that the point distribution in the field was not always optimal. In order to overcome this problem, a solution based grid adaptation was used for all further calculations.

8.5.2 Solution Based Grid Adaptation

The solution based grid adaptation was realized by the use of the adaptation technique, which is included in the DLR-TAU Code (Refs. [8-7]-[8-9]). The adaptation algorithm needs a hybrid grid and a matching flow solution. With the aid of refinement sensor functions it is determined which edges of the primary grid have to be bisected. As sensor functions the differences of the flow variables between the edge points along an edge were applied, and as flow variables the magnitude of the velocity, the density, the total pressure, and the helicity were used. During the adaptation points can be added and removed, but only points which have been previously added can be removed. The adaptation is a static grid refinement, which can be started after the computation of a flow solution on a certain grid. It then generates a new primary grid and interpolates the solution onto this grid. This procedure can be repeated several times in order to get a final adapted grid.

The starting grid for the solution based grid adaptation was generated by the "CentaurSoft" grid generator [8-6] as described above. This initial grid had 10496522 nodes in total for the half-span full-scale model of the F-16XL. It had a prismatic layer of 15.6 million prisms in the near wall region and 13.5 million tetrahedra in the outer region. The thickness of the first prismatic layer was 4.0e-06 m and a geometric progression parameter of 1.3 was used for the other 29 viscous layers. In critical regions the prismatic layers were chopped and transition elements such as pyramids and tetrahedra were created. The surface of the aircraft was resolved by 749742 triangles.

This grid was adapted in 4 steps for each flight condition. The maximum increase of grid points for each of the 4 adaptation loops was limited to 25%. Grid points have been added in the surface grid and in the tetrahedral grid. The new surface points have been included in the prismatic grid, but number and thickness of the prismatic layer have not been changed. (The initial prismatic layer was designed such, that it was suitable for a much finer grid).

With this adaptation procedure the final adapted grid (for example FC 25) obtained 1462096 surface triangles, 32375977 prisms, and 258771331 tetrahedra. Compared to the initial grid, these elements roughly have been doubled, resulting in a total number of 21149945 nodes. Figure 8-2 shows the development of the surface grid during the 4 adaptation steps. New grid points mainly have been added along the leading edge (leading edge suction), inboard and outboard of the suction peak of the primary vortex (pressure gradient) and in the tip section of the rearward wing.

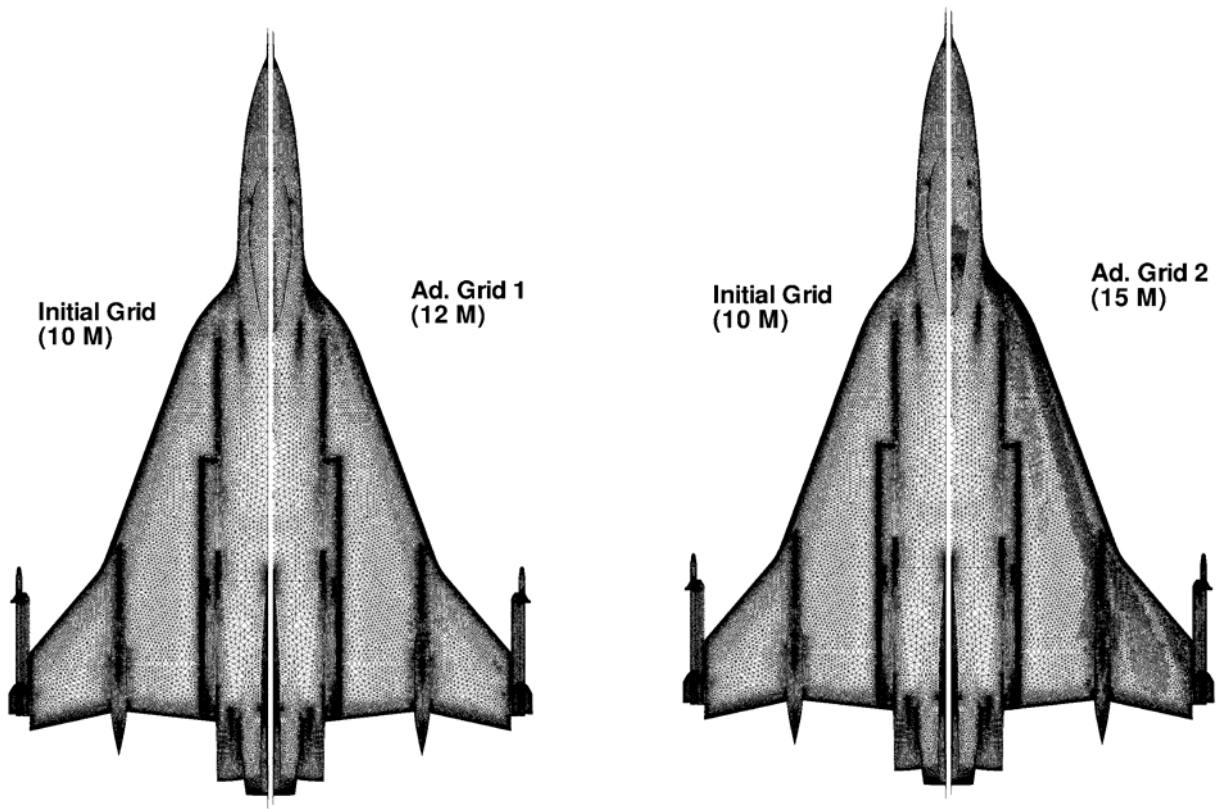

(a) First Adaptation Step **(b) Second Adaptation Step**

Figure 8-2: Surface Grid Adaptation for FC 25 (M_∞ = 0.242, α = 19.84°, Re = 32.22 x 10^6).

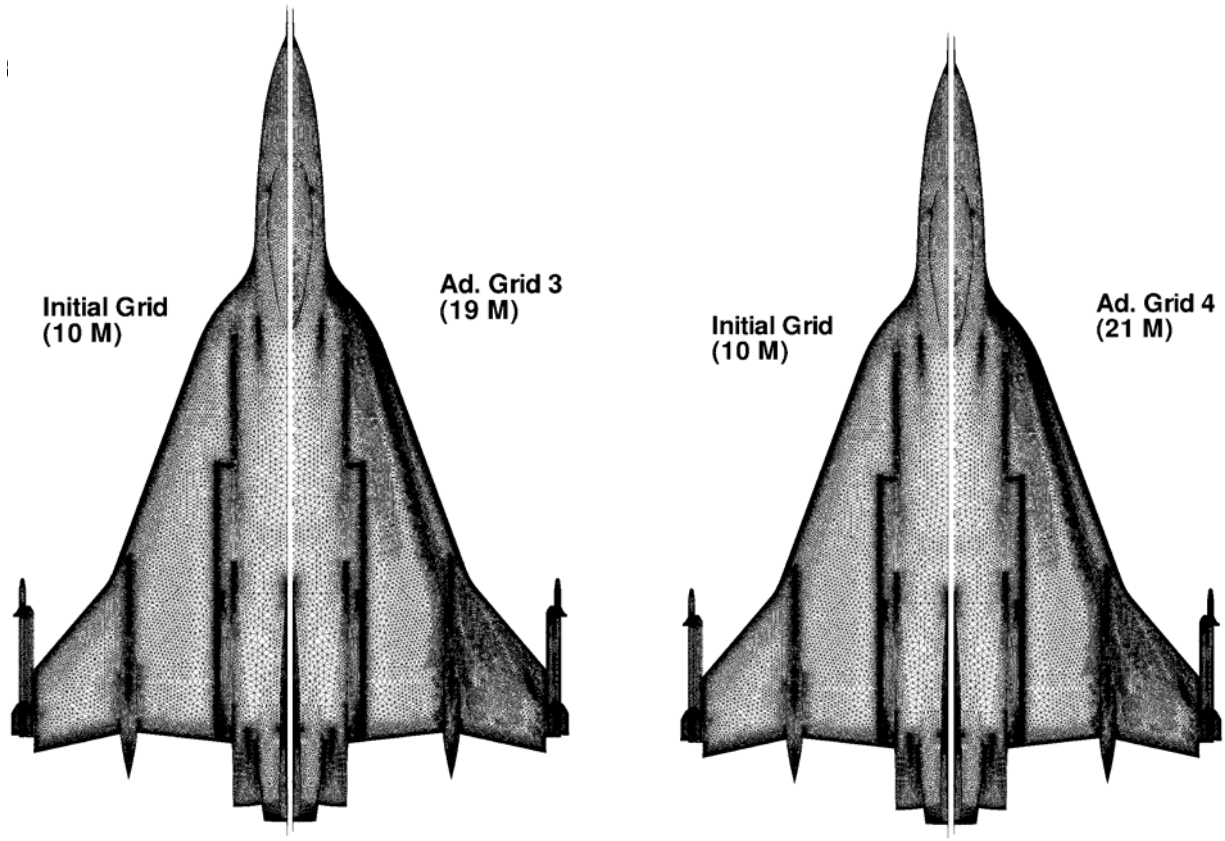

(c) Third Adaptation Step **(d) Fourth Adaptation Step**

Figure 8-2: Concluded.

In space, new points have been added in regions with vortical flow above the wing (total pressure, helicity) and in the wake region behind the wing, as it is demonstrated in Figure 8-3 for FC 25 at two different cross sections.

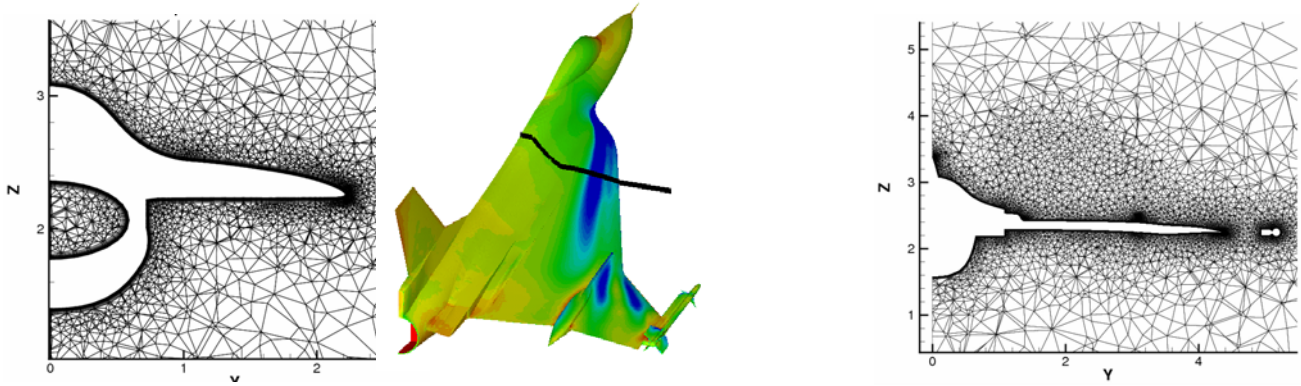

(a) Initial Grid

(b) Initial Grid

(c) First Grid Adaptation

(d) First Grid Adaptation

(e) Second Grid Adaptation

(f) Second Grid Adaptation

Figure 8-3: Field Grid Adaptation for FC 25 (M_∞ = 0.242, α = 19.84°, Re = 32.22 x 10^6).

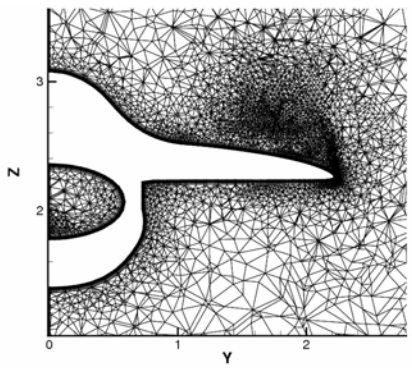

(g) Fourth (Final) Adaptation

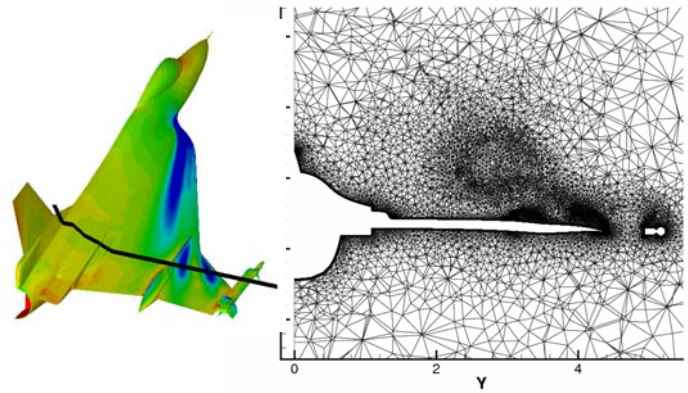

(h) Fourth (Final) Adaptation

Figure 8-3: Concluded.

Figure 8-4 shows a comparison between a so called "manually adapted" grid (left hand) and the final solution adapted grid for FC 25. In the manually adapted grid the grid points are concentrated in regions where a priori vortices were expected.

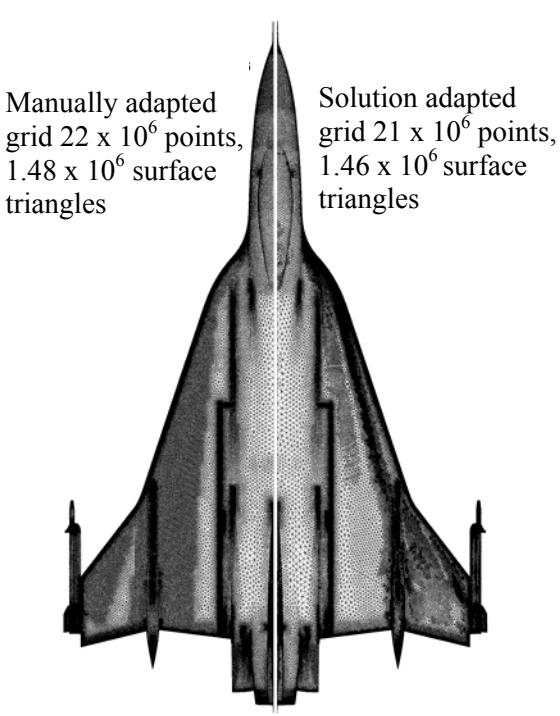

(a) Surface Grid

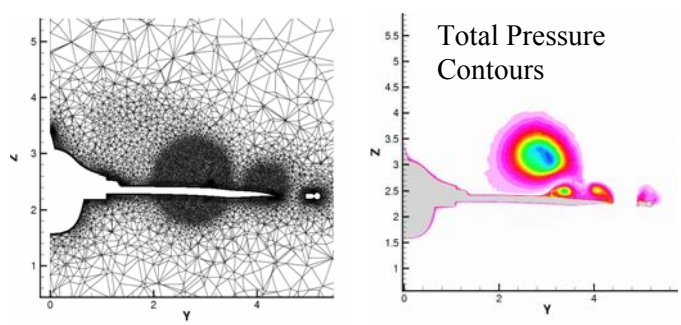

(b) Manually Adapted Grid at x = 11 m

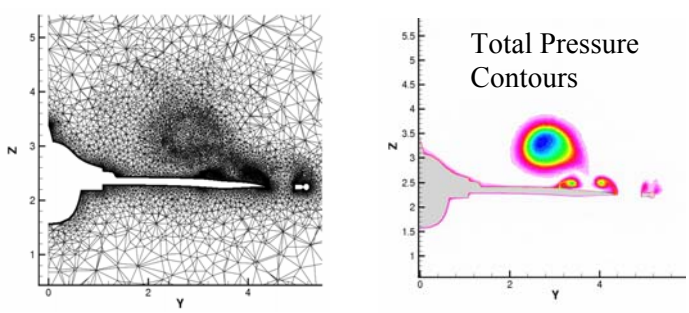

(c) Solution Adapted Grid at x = 11 m

Figure 8-4: Manually and Solution Adapted Grid for FC 25 (M_∞ = 0.242, α = 19.84°, Re = 32.22 x 10^6).

Both grids have approximately the same grid size and also nearly the same number of surface triangles, but the point distribution is completely different. In the flow solution for FC 25 it turned out, that the leading edge vortex moved outside of the high resolution region of the grid (Figure 8-4 (b)) and smeared out. By this the leading edge suction peaks were under predicted in the calculation. With the solution adapted grid, the vortices were caught by the grid which resulted in much more compact vortices (Figure 8-4 (c)).

Figure 8-5 illustrates the convergence of the surface pressure distribution during the four adaptation steps at two different wing sections for FC 25. Obviously the pressure distributions shift towards a final distribution. As there is nearly no difference between the result of the third adaptation and the fourth adaptation, it can be concluded, that the results after the fourth adaptation can be considered as final results.

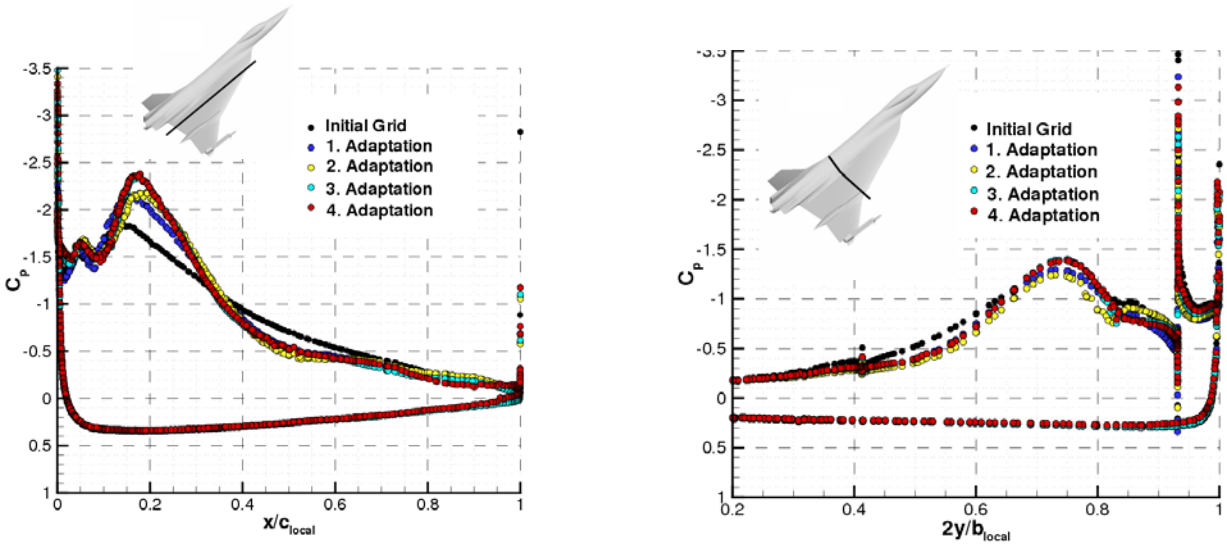

Figure 8-5: Convergence of Surface Pressure Distribution during the Grid Adaptation for FC 25, (M_∞ = 0.242, α = 19.84°, Re = 32.22 x 10^6).

8.6 FLOW SOLUTION

All flow solutions were obtained by the use of the DLR flow solver TAU (Refs. [8-7], [8-8]).The TAU-code is a software system consisting of several separate modules for the prediction of viscous and inviscid flows about complex geometries employing hybrid unstructured grids. In the actual calculations, the modules for pre-processing (computation of the dual grid, metrics, and connectivity), the flow solver and the adaptation module have been used. The pre-processing had to be run for each new primary grid, i.e. also after each adaptation step. The flow solver module uses an edge-based dual cell approach, where the inviscid terms are computed either by a second-order central scheme or a variety of upwind schemes. For the time integration various explicit Runge-Kutta schemes or the explicit LU-SGS (Lower-Upper Symmetric Gauss-Seidel) scheme can be employed. Convergence acceleration is achieved by a multi-grid algorithm based on agglomerated coarse grids. To allow for turbulence, different one- and two-equation turbulence models as well as DES are available.

In the actual flow calculations, the flow solver was applied with the AUSMDV upwind scheme, backward Euler implicit time integration (solved by LU-SGS), SAE one-equation turbulence model, and a 3W multi-grid convergence acceleration. For the initial solution 8000 multi-grid cycles were run and additional

4000 cycles after each adaptation step. The flow solutions were run on 32 processors of a 128/2 Linux cluster (2.6 GHz/CPU). This resulted in a CPU-time of 13h per 1000 MG-cycles and in a turnaround time of 2 – 3 weeks for each test case (starting from scratch, 4 grid adaptations, including all trial and error loops).

Some test calculations using the rotational correction of the turbulence model (SARC) have shown a considerable effect on the eddy viscosity distribution but no effect on the global flow characteristics (pressure distribution, total pressure distribution, vortical flow structure). Other experiences at EADS-MAS with similar configurations have shown that in fine grids the rotational correction limits the eddy viscosity too much, so that the solution can become unstable and has to be stabilized by high artificial viscosity. By this reason the SAE and not the SARC turbulence model was used for the calculations.

8.7 RESULTS AND DISCUSSION

8.7.1 Flight Condition 7

Figure 8-6 shows the surface pressure contours obtained in the manually adapted grid and in the final solution adapted grid (Figure 8-6 (b)). In Figure 8-6 (a) the two different grids are represented. Both grids are of similar size, but the point distribution is very different.

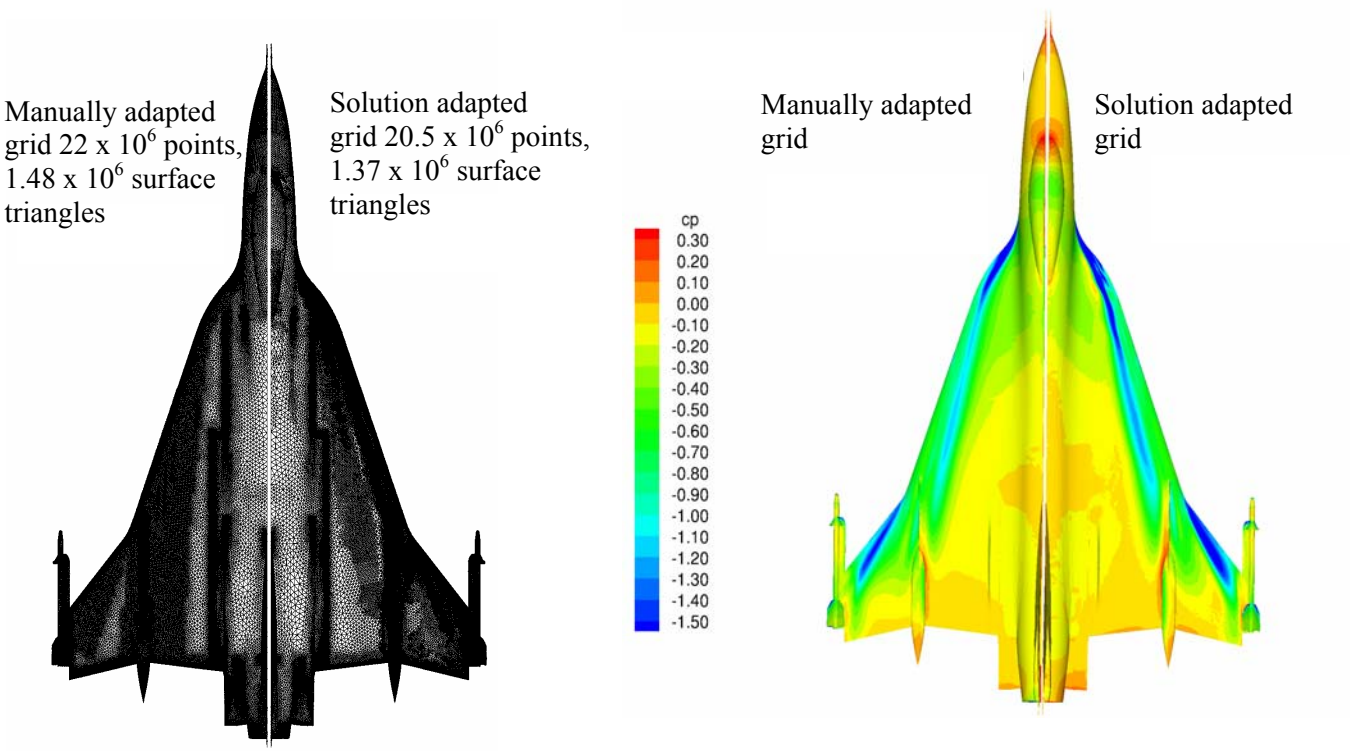

(a) Surface Grids **(b) Surface Pressure Contours**

Figure 8-6: Surface Grids and Surface Pressure Contours for FC 7 (M_∞ = 0.304, α = 11.89°, Re = 44.4 x 10^6).

The solution based grid adaptation has concentrated the grid points at the wing apex, along the leading edge and inboard and outboard of the leading edge suction peak. The reason for the concentration at the wing apex

is the cropped sharp leading edge of the wing, which induces high values of the sensor function for the adaptation (at the surface and in the field).

The pressure contours of the solution adapted grid indicate stronger and more compact leading edge vortices inboard and outboard of the crank. In the apex region of the wing, the solution adapted grid shows two additional small suction peaks between the leading edge and the main leading edge vortex. This may be related to the shape of the leading edge in this region. The cropped sharp leading edge produces pressure disturbances and the finer the grid resolution, the more such disturbances appear in the solution. Or those disturbances are damped out by a high natural or numerical viscosity, as it is indicated by Figure 8-7.

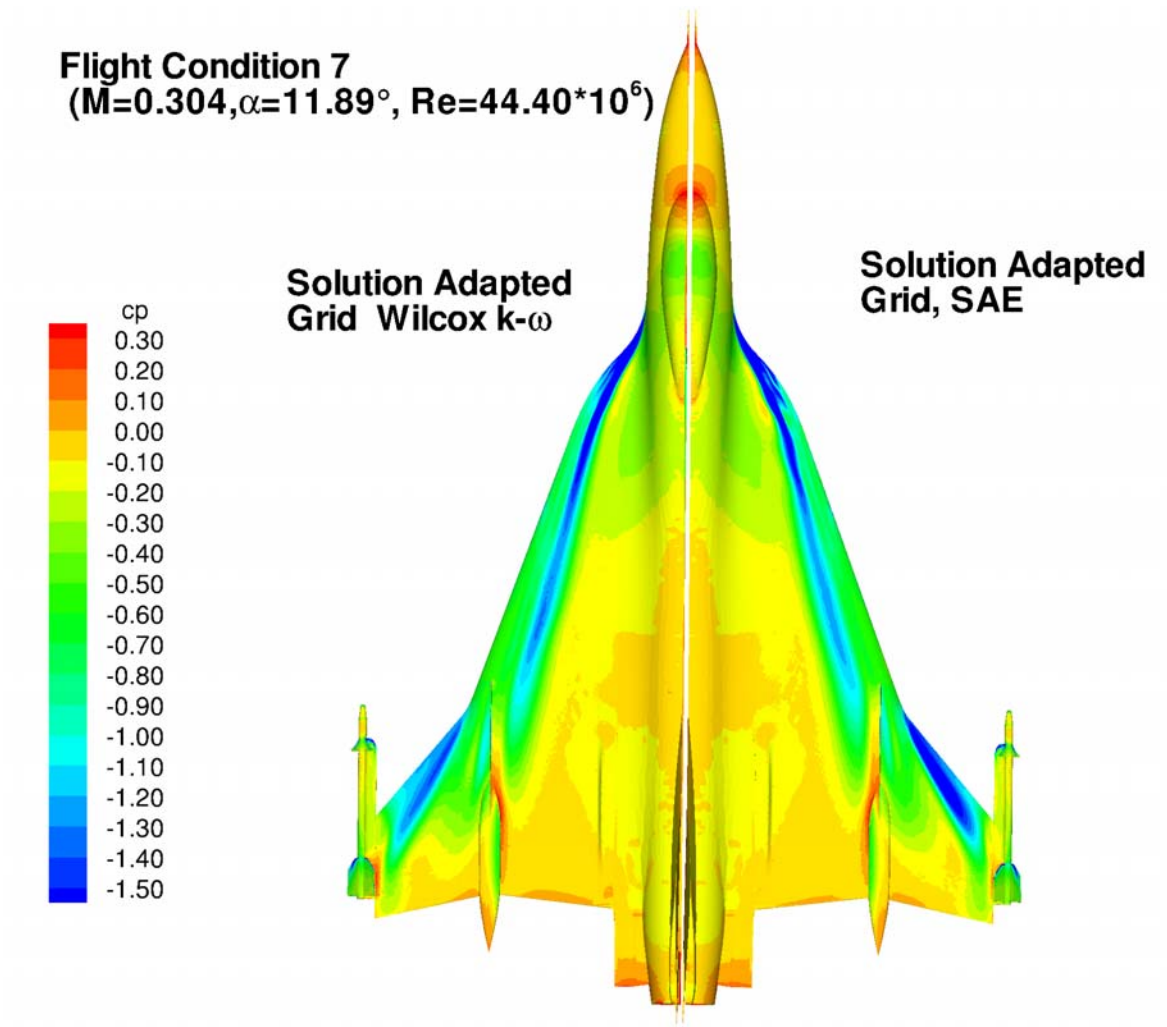

Figure 8-7: Effect of Turbulence Model on Surface Pressure Distribution at FC 7.

A solution with the Wilcox k-ω turbulence model (which is more dissipative than the SAE-model) does not show these pressure disturbances in the apex region of the wing. The k-ω model gives also a weaker leading edge vortex outboard of the crank, whereas the suction peak inboard of the crank sows no substantial difference to the SAE solution.

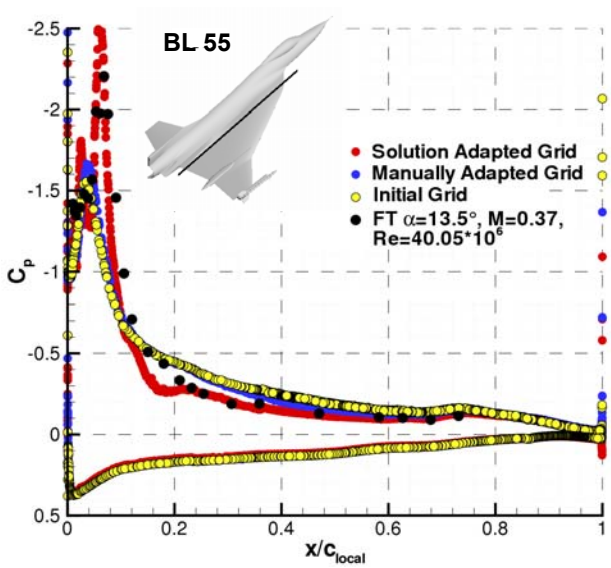

(a) BL 55

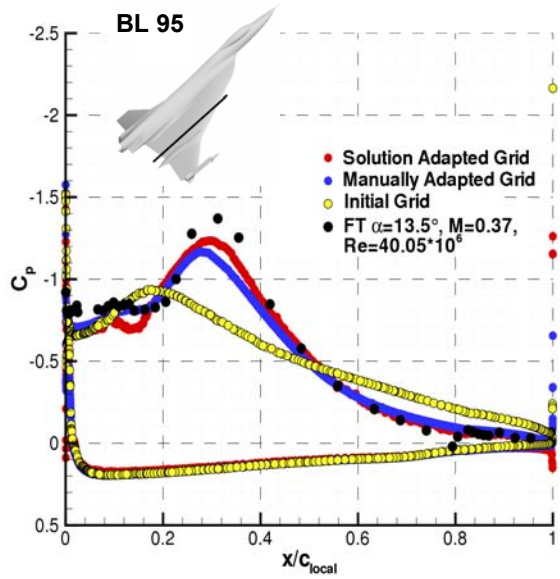

(b) BL 95

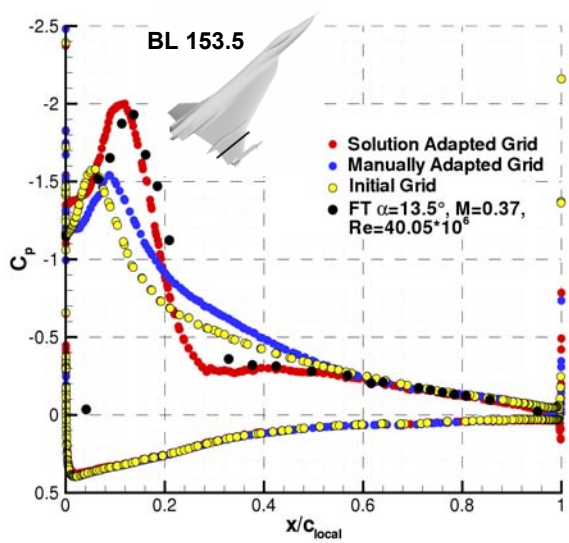

(c) BL 153.5

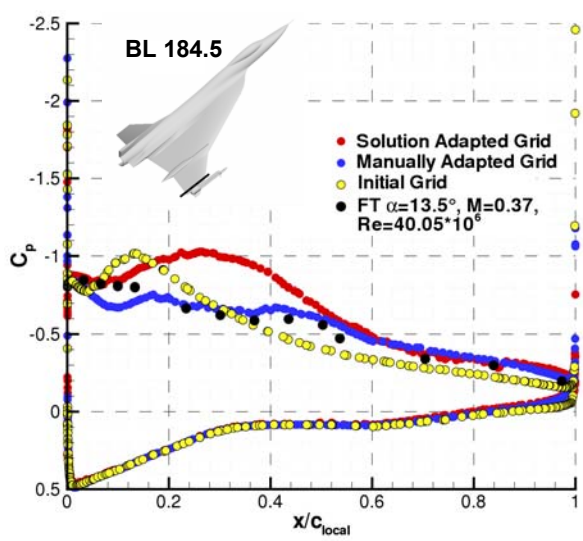

(d) BL 184.5

Figure 8-8: Surface Pressure Distributions at Wing Sections y = constant for FC 7 (M_∞ = 0.304, α = 11.89°, Re = 44.4 x 10^6).

It should be mentioned, that for FC 7 only boundary layer data but no pressure data from flight test were available. The numerical results in Figure 8-8 are therefore compared with a flight condition, which is very close to FC 7 (the substantial difference is the angle of attack, which is in the flight test 1.5 degrees higher than in the calculation). Figure 8-8 shows the results of 3 different computational grids: the initial grid (yellow symbols), the manually adapted grid of Figure 8-4 (blue symbols), and the solution based adapted grid (red

symbols). Except at the most outboard wing section, the agreement of the results oft the solution adapted grid with the flight test data is pretty good. There is a clear difference between the results of the initial grid and those of the solution adapted grid. At the section BL 95 (Figure 8-8 (b)) the results of the manually adapted grid and of the solution adapted grid are very close, but in all other sections there are considerable differences. At the section BL 55 the solution adapted grid shows this above mentioned second peak very close to the leading edge, which is not present in the flight test data.

The surface pressure distributions in two cross-sections x = constant are given in Figure 8-9. Unfortunately the flight test data points are not very dense, but Figure 8-9 indicates, that the results of the solution adapted grid give the correct position and the correct level of the leading edge suction peak. Remarkable is the clear difference between the two fine grids and the initial grid.

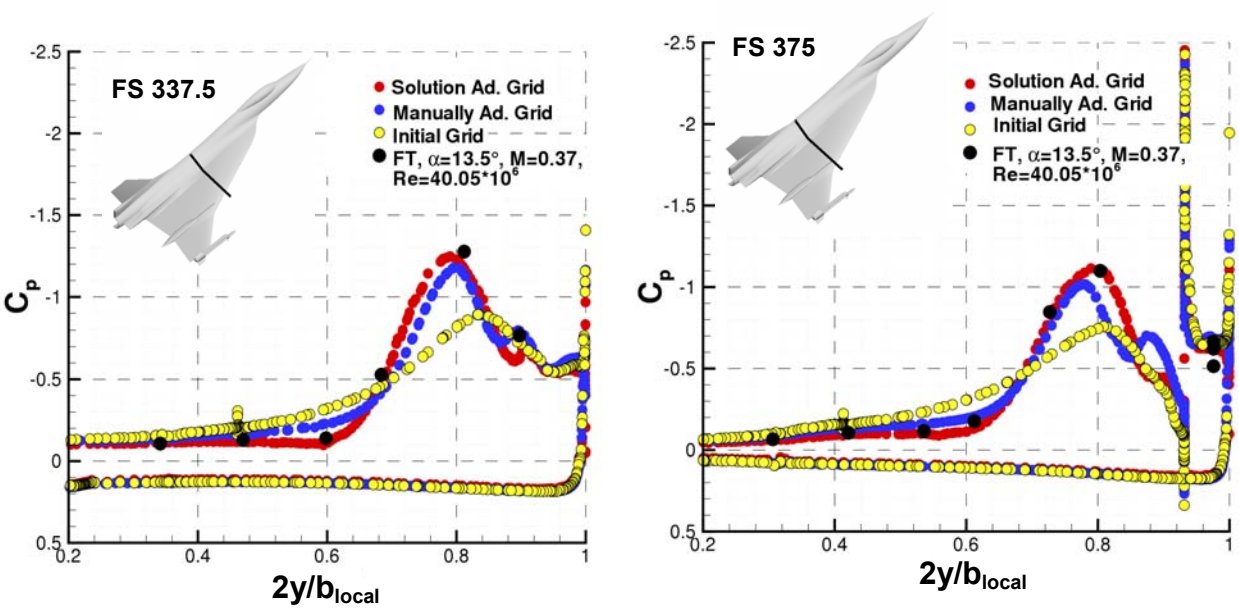

(a) FS 337.5 **(b) FS 375**

Figure 8-9: Surface Pressure Distributions at Cross-Sections x = constant for FC 7 (M_∞ = 0.304, α = 11.89°, Re = 44.4 x 10^6).

Figure 8-10 shows the boundary layer comparison between the measured and predicted data at 4 different positions. (v_e is the velocity at the rake extreme total pressure tube). Rake 3 (Figure 8-10 (a)) is inboard of the primary vortex and should be in basically stream wise flow. Here the predicted data show the effect of too much turbulence and this effect is independent of the two different turbulence models. Rake 4 is beneath the primary vortex (Figure 8-10 (b)) and the agreement between experiment and numerical predictions is pretty good. The k-ω solution shows the effect of somewhat more turbulence compared to the SAE solution and the experimental results. Rake 5 and rake 7 are both outboard of the primary vortex and very close to each other. (Rake 5 is a little bit more outboard than rake 7). Whereas rake 5 shows a very good agreement between numerical and experimental data, there is a considerable defect in the predicted velocity profiles at rake 7.

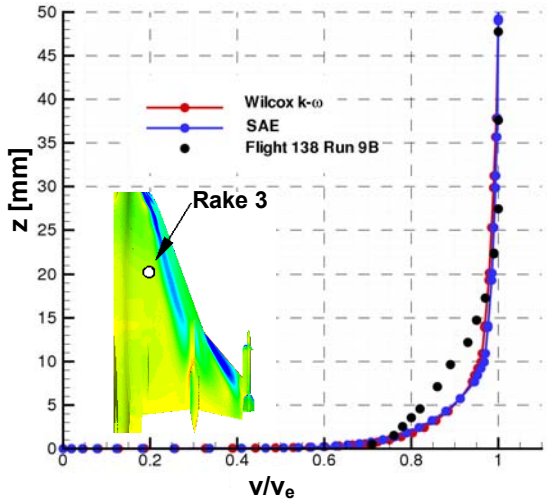

(a) Rake 3

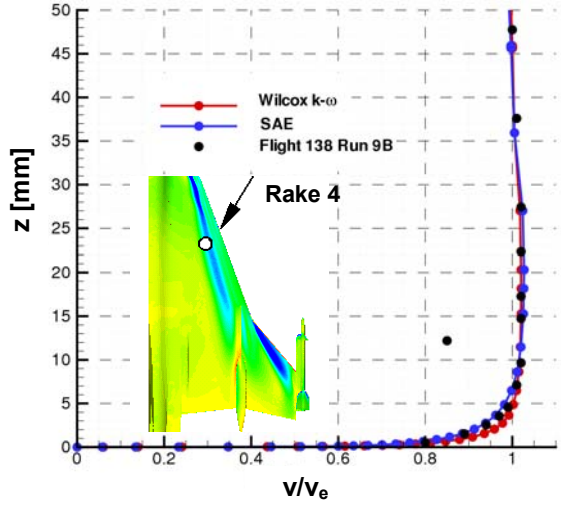

(b) Rake 4

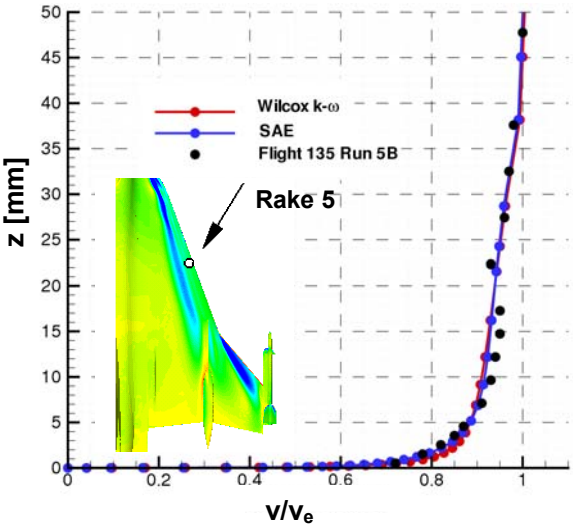

(c) Rake 5

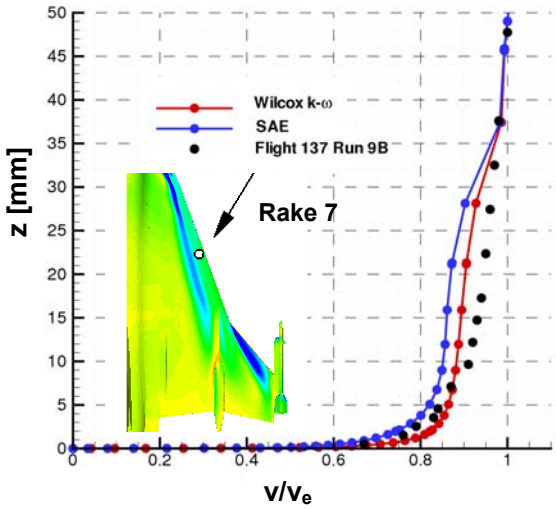

(d) Rake 6

Figure 8-10: Comparison of Boundary Layer Profiles with Flight Measurements for FC 7 (M_∞ = 0.304, α = 11.89°, Re = 44.4 x 10^6, Solution Adapted Grid).

8.7.2 Flight Condition 19

FC 19 is very close to the previous FC 7 and thus the final adapted grid of FC 7 was also used for FC 19. Figure 8-11 shows a comparison of computed and measured local skin friction coefficient at the cross-section x = constant.

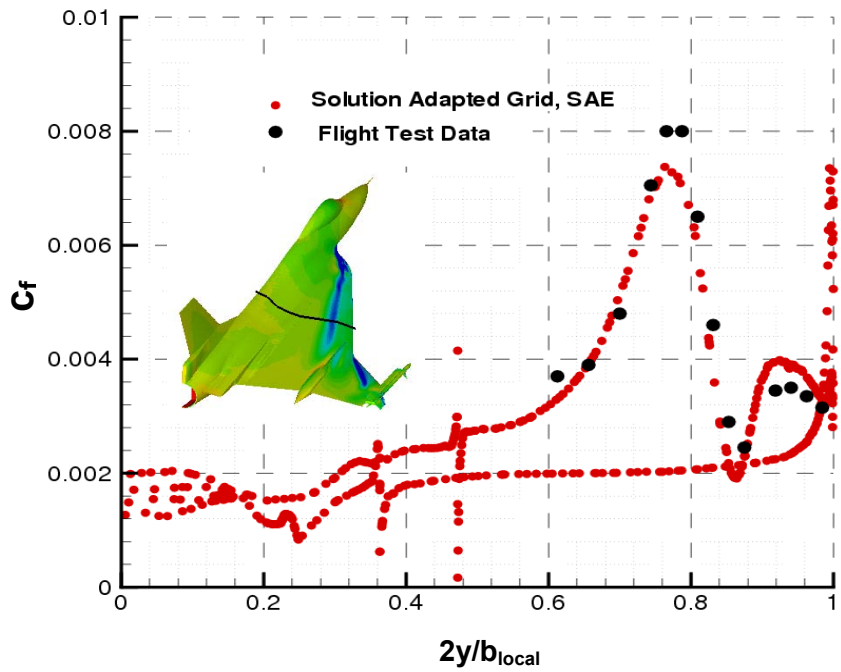

Figure 8-11: Comparison of Predicted and Measured c_f for FC 19 (M_∞ = 0.36, α = 11.85°, Re = 46.8 x 10^6).

There are two peaks in the skin friction distribution. The smaller one, close to the leading edge, indicates the presence of a secondary vortex and the higher one indicates the presence of a primary vortex above the surface. The level associated with the primary vortex is not exactly reached by the calculation, but the span wise location is perfectly matched. The second peak is slightly over predicted.

8.7.3 Flight Condition 25

FC 25 is the flight condition with the highest angle of attack and thus a challenging test case. For this FC pressure data from flight test were available. The grids which have been used for this FC are described in the section IV.B (Solution based grid adaptation) and are shown in details in Figure 8-2, Figure 8-3, and Figure 8-4. Figure 8-12 shows the surface pressure contours obtained in the manually adapted and in the solution based adapted grid.

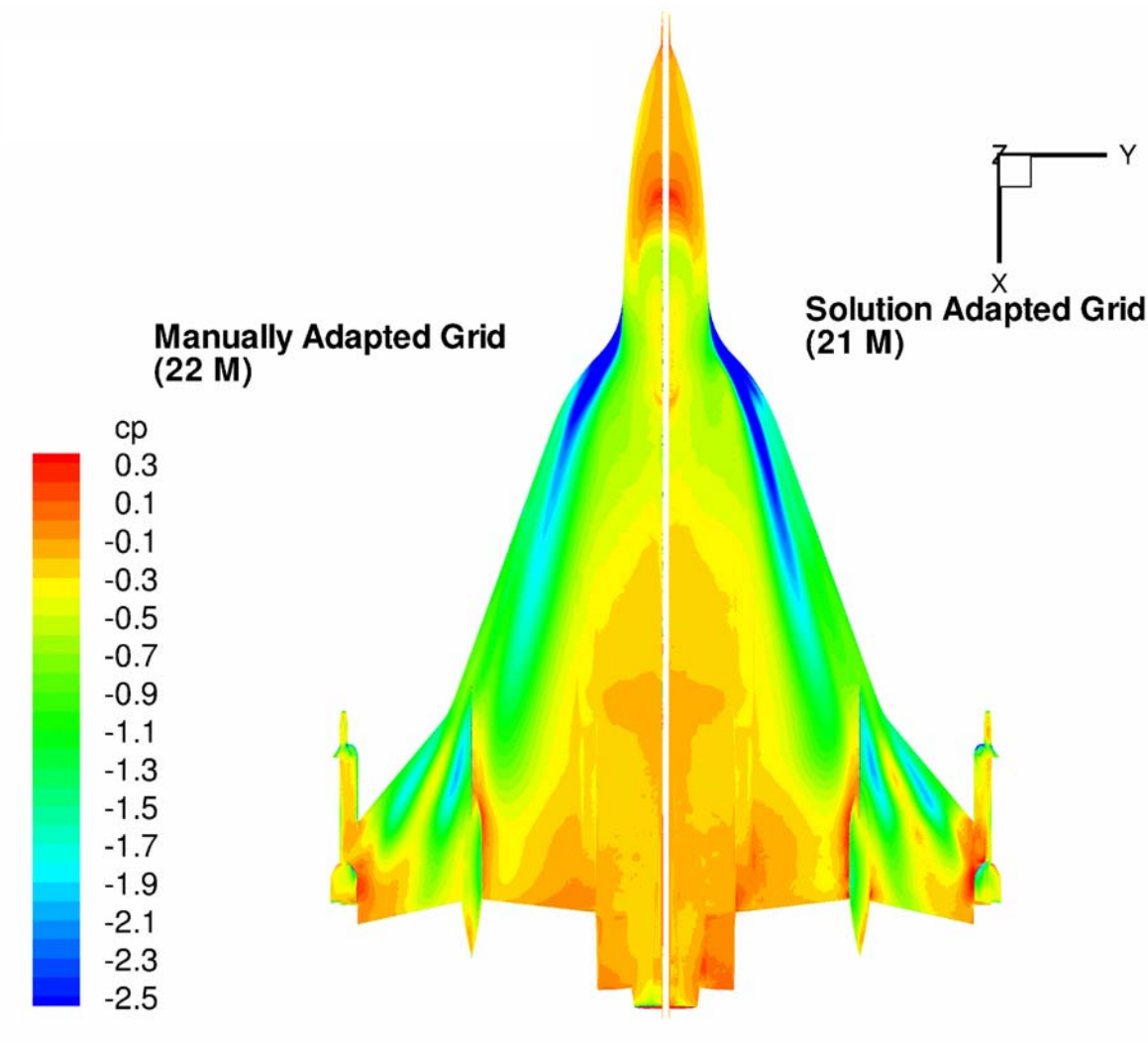

Figure 8-12: Surface Pressure Contours for FC 25 (M_∞ = 0.242, α = 19.84°, Re = 32.22 x 10^6).

The tendency is similar as it was observed for FC 7: in the solution adapted grid there is a stronger and more compact primary vortex at the inner wing. There is also a rather strong effect of the airdam. At the inboard side of the airdam and the actuator pod, there is deceleration of the flow and at the outboard side, a new vortex is generated. Considering the main primary vortex, it can not be concluded from the surface pressure contours, whether there is vortex break down or not.

Figure 8-13 shows a comparison of predicted and measured surface pressure distributions for different wing sections (BL) and cross sections (FS).

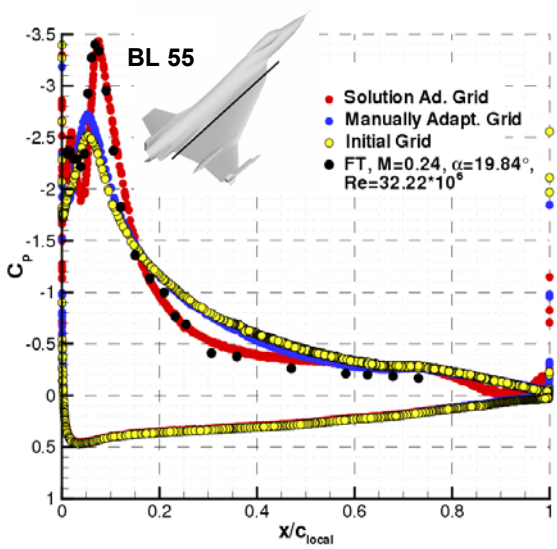

(a) BL 55

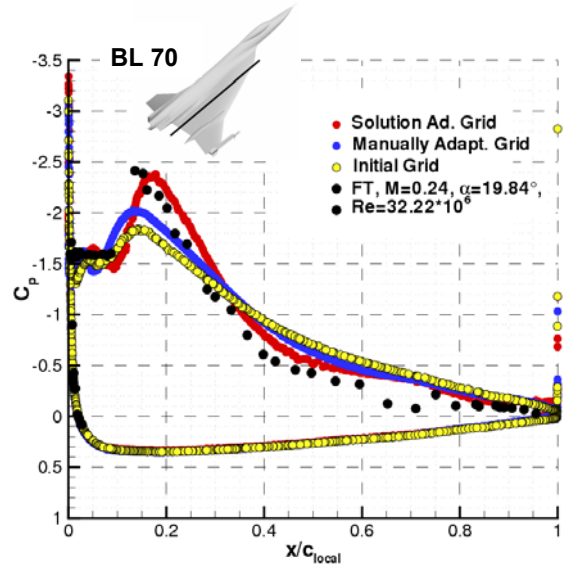

(b) BL 70

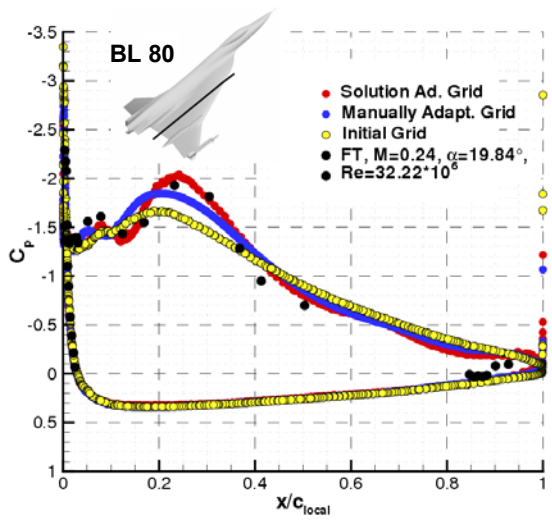

(c) BL 80

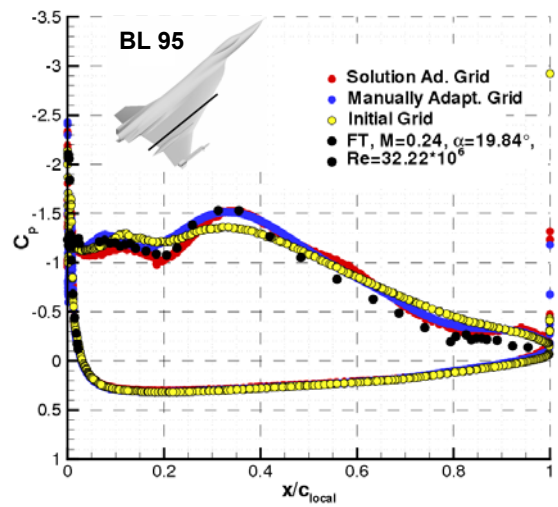

(d) BL 95

Figure 8-13: Computed and Measured Surface Pressure Distribution at FC 25 (M_∞ = 0.242, α = 19.84°, Re = 32.22 x 10^6).

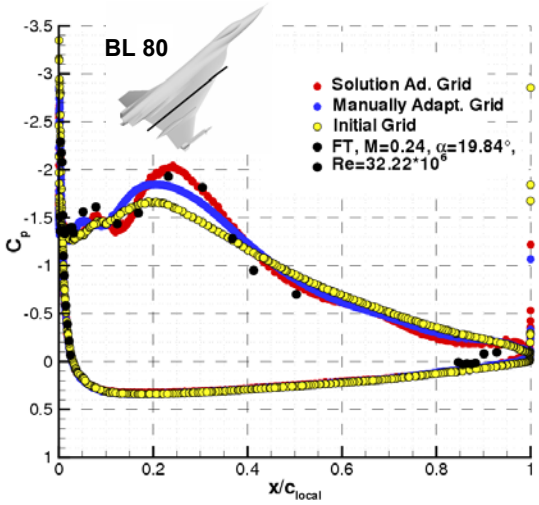

(d) BL 80

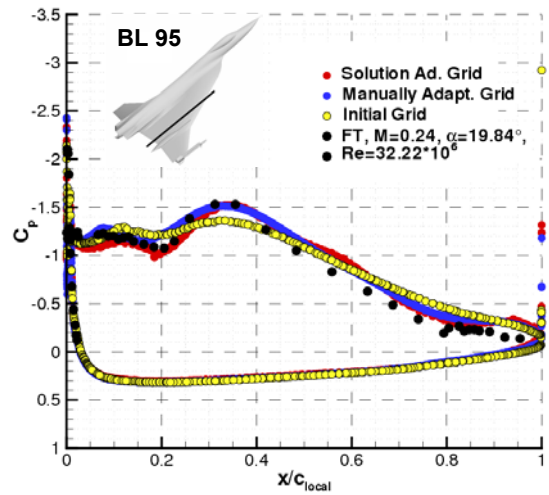

(e) BL 95

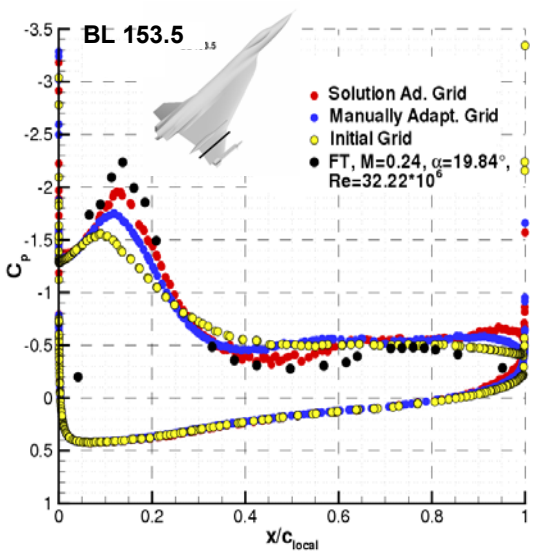

(f) BL 153.5

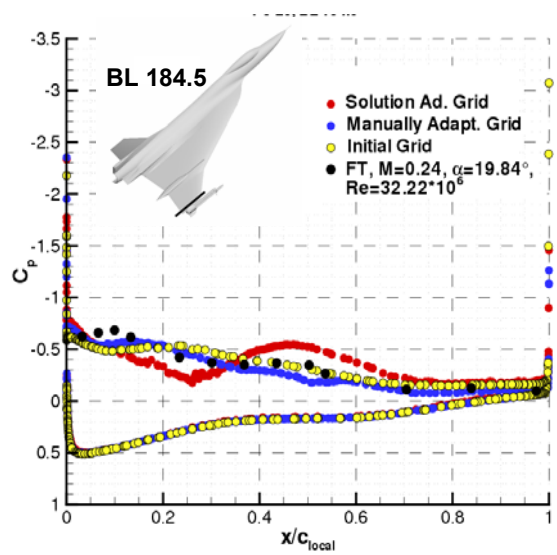

(g) BL 184.5

Figure 8-13: Continued.

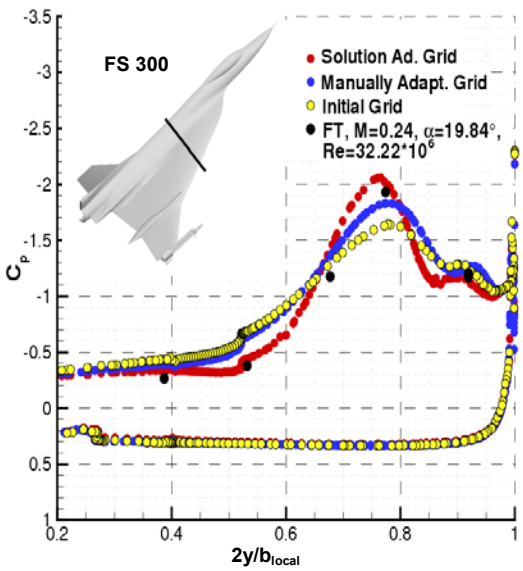

(g) FS 300

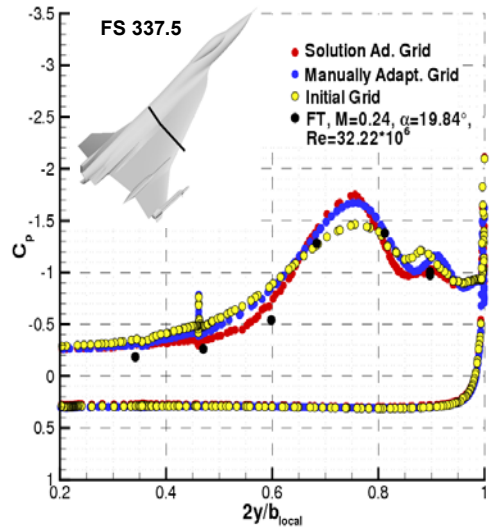

(h) FS 337.5

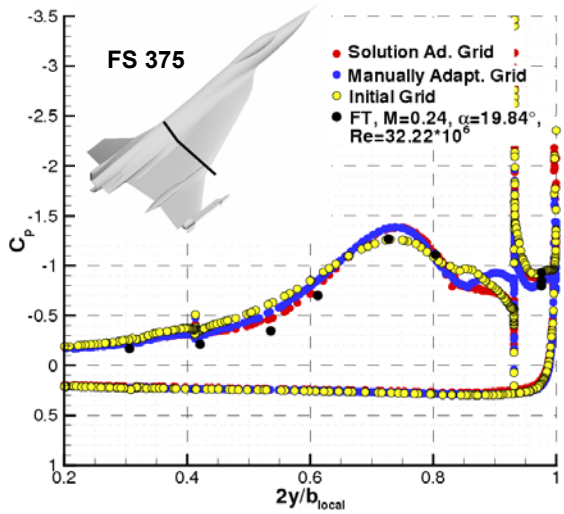

(i) FS 375

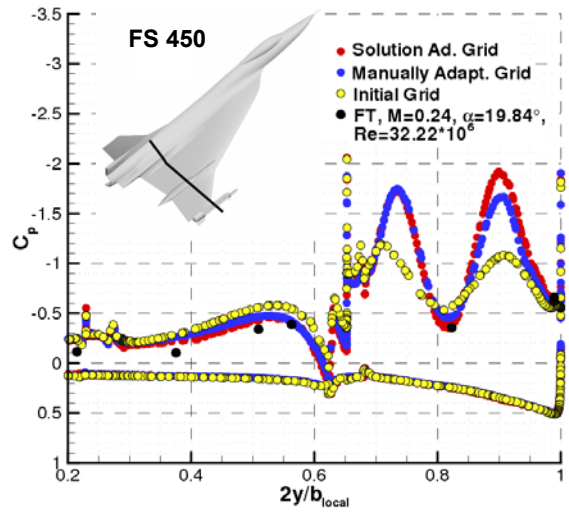

(j) FS 450

Figure 8-13: Concluded.

As can be seen, the results of the solution adapted grid show a very good agreement with the measured data. Only at BL 153.5 (Figure 8-13 (e)) there is a slight under prediction of the suction peak. The secondary vortex is also very well predicted. There are clear differences between the solution adapted grid and the other grids. The initial grid is of course not fine enough, but also the manually adapted grid with its 22 million grid points was not suitable for this FC. The reason for it is given in Figure 8-4: the leading edge vortices move outside of the high resolution region of the grid. By this the vortices weaken, which results in an under prediction of the suction peaks. In the solution adapted grid, the vortices were caught; they keep compact and are not smeared out.

The pressure distributions in the cross sections (Figure 8-13 (g), Figure 8-13 (h), and Figure 8-13 (i) show very clearly the presence of a primary and secondary vortex until to the beginning of the airdam. With the beginning of the airdam there are 3 vortices. Inboard of the airdam there is the remainder of the primary vortex, which is no longer fed by the leading edge and thus it weakens more and more. The two outboard vortices, which can also be recognized in the surface pressure contours (Figure 8-12), are induced by the airdam and by the crank in the wing.

Figure 8-14 shows the total pressure loss contours and gives some insight into the vortical structure of the flow field. At the apex of the wing a primary vortex develops, which moves inboard and upward of the wing when going in stream wise direction. Thereby the vortex core moves more and more away from the leading edge and the feeding of the vortex by the leading edge becomes weaker and weaker. With the beginning of the airdam, the primary vortex loses the connection to the leading edge and is no longer fed by it. As a consequence the primary vortex becomes weaker and dissipates downstream of the wing, but it does not look like vortex break down. (There is a continuous decrease of the total pressure loss in the vortex core, but the vortex core seems to remain compact). Due to the sidewash of the primary vortex, there is outboard directed flow at the airdam. This outboard directed flow crosses the airdam and induces a new vortex, which turns in opposite direction as the wing primary vortex. At the crank, the sharp leading edge of the outer wing induces a new primary vortex, which turns in the same direction as the wing primary vortex. Upstream of the airdam there is a secondary vortex beneath the primary vortex. Between the secondary vortex and the wing leading edge, there is another vortex. It has the same rotational direction as the primary vortex and can be considered as an elementary part of the feeding sheet of this primary vortex. Behind the wing, the airdam vortex, the outboard wing leading edge vortex and the missile induced vortices merge into one common vortex.

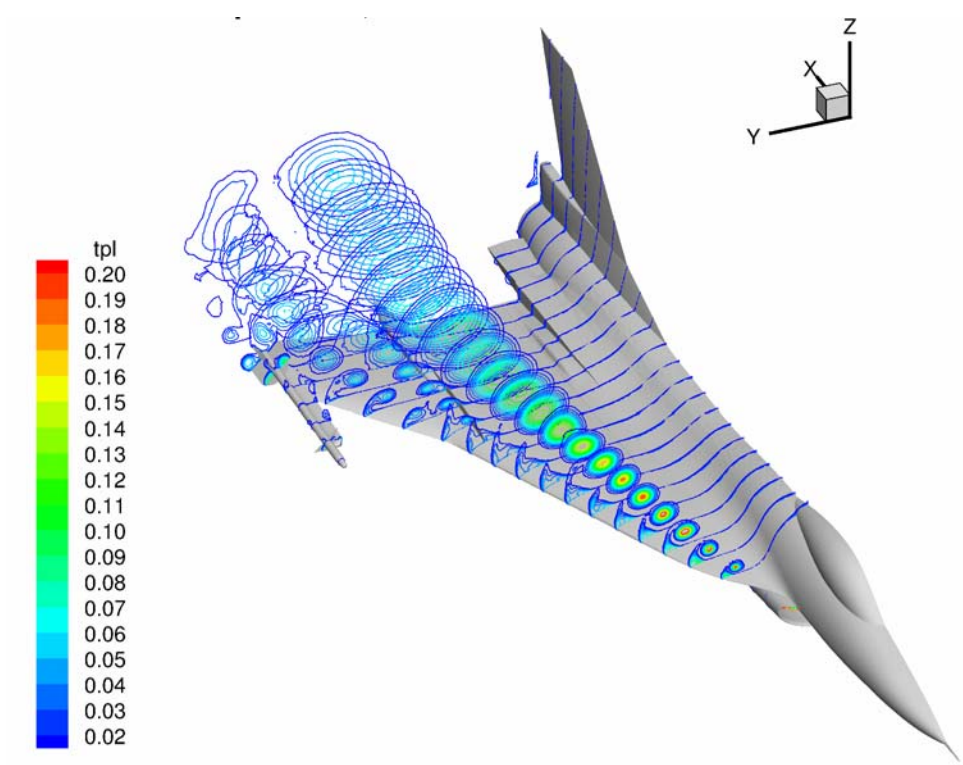

Figure 8-14: Total Pressure Loss Contours at FC 25 (M_∞ = 0.242, α = 19.84°, Re = 32.22 x 10^6).

Figure 8-15 shows some more details of the flow structure at the airdam and at the actuator pod. Upstream of the airdam, the primary vortex and the secondary vortex as well as the small vortex between secondary vortex and leading edge with their separation and attachment lines can be found very clearly in the skin friction lines. Figure 8-15 also shows the interaction of the secondary vortex with the airdam more detailed. The airdam divides the secondary vortex into a small outboard part and into a main part, which remains inboard of the airdam. The outboard part merges into the airdam vortex, whereas the inboard part serves the outboard directed flow as a ramp to ease the crossing of the airdam.

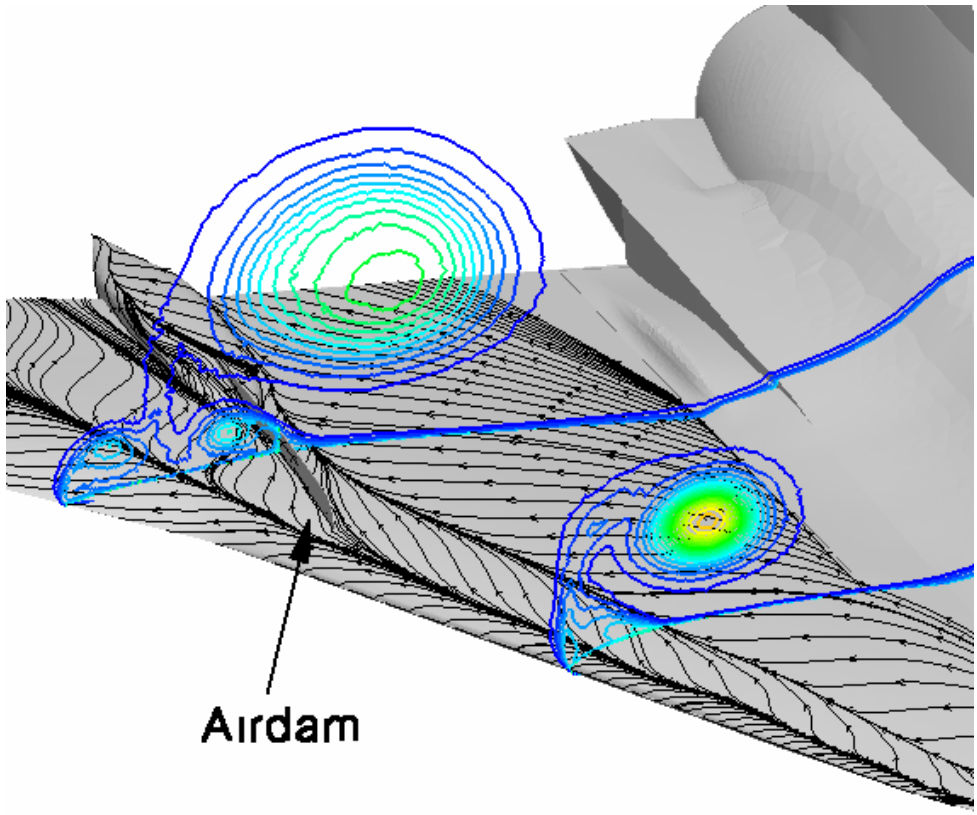

Figure 8-15: Surface Skin Friction Lines and Total Pressure Loss Contours at FC 25 (M_∞ = 0.242, α = 19.84°, Re = 32.22 x 10^6).

8.7.4 Flight Condition 70

This flight condition is characterized by a high, transonic Mach number, but low incidence. Thus no dominating vortical flow characteristics but transonic flow with shocks are to be expected for this test case. Also for this test case the manually adapted grid and the solution adapted grids have been employed in the calculations. The manually adapted grid and the initial grid for the adaptation are the same as for the other flight conditions. Figure 8-16 gives a comparison of the manually adapted grid and the final solution adapted grid.

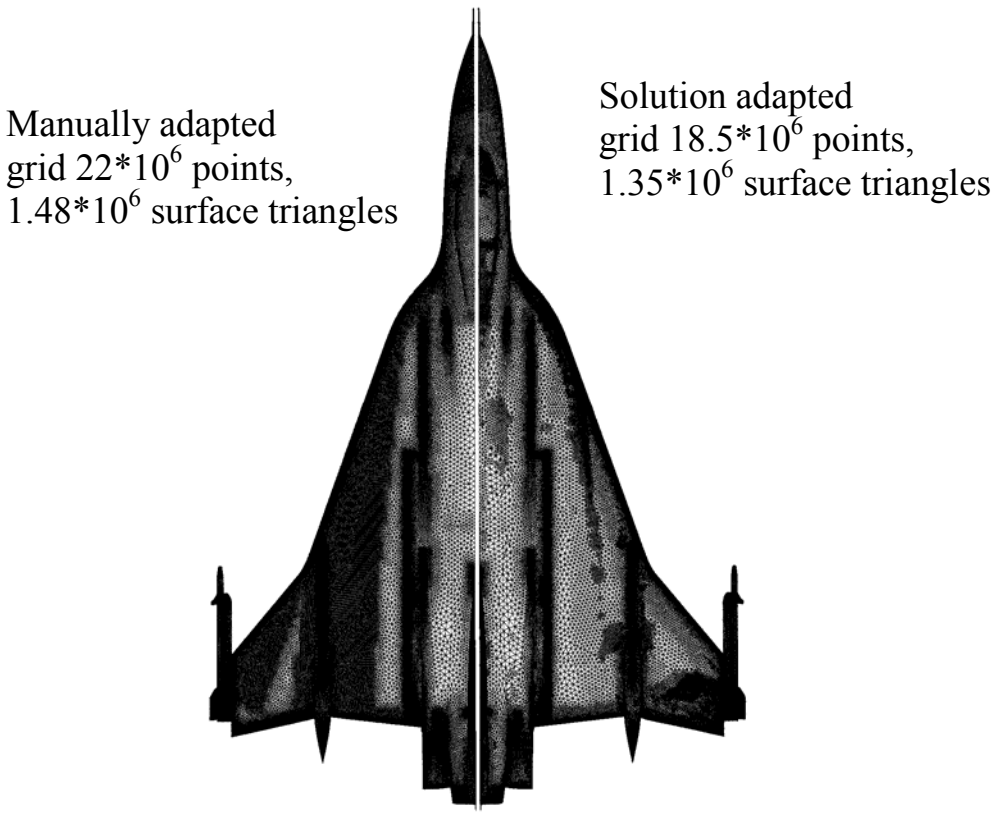

Figure 8-16: Grids for FC 70 (M_∞ = 0.97, α = 4.37°, Re = 88.77 x 10^6).

The final adapted grid (right hand in Figure 8-16) does not show specific transonic flow characteristics. Points have been added in the wing apex region, along the wing leading edge, along the airdam and the actuator pod, and in the region close to the missile. Only at the canopy there is a shock-wave type concentration of grid points.

The surface pressure contours of Figure 8-17 show a surprising result: although the 3 grids are very different, there is no substantial difference in the surface pressure contours. There is a shock wave at the canopy and after the first third of the wing; both are present in the solutions of all grids. In the first third of the wing there is also the footprint of a very weak leading edge vortex. In the solution of the manually adapted grid (Figure 8-17 (b)) this vortex crosses the shock wave clearly, in all other solutions it indeed crosses the shockwave, but then it dissipates.

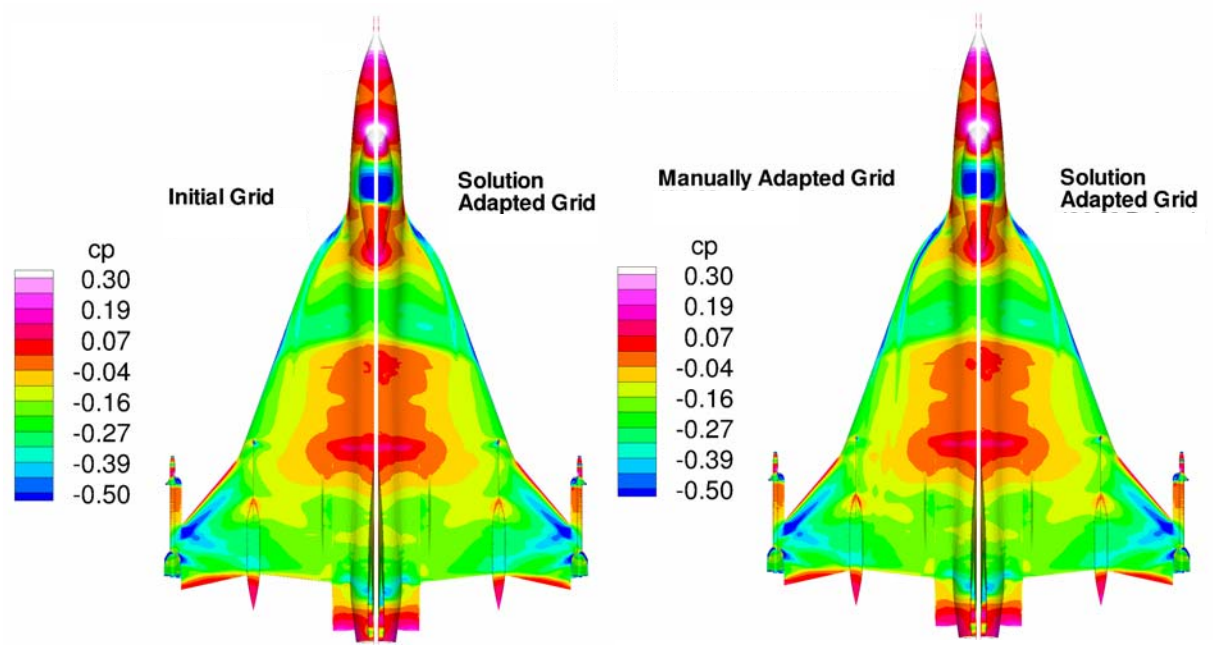

(a) Initial and Solution Adapted Grid **(b) Manually and Solution Adapted Grid**

Figure 8-17: Computed Surface Pressure Contours in Different Grids at FC 70 (M_∞ = 0.97, α = 4.37°, Re = 88.77 x 10^6).

Figure 8-18 shows a comparison of computed and measured surface pressure distributions. It is obvious, that the pressure distributions obtained in the different grids are more or less identical and it is also obvious that except at BL 55 (Figure 8-18 (a)), the numerical data do not match the measured data. In the numerical results there is the above mentioned shock wave at the end of the first third of the wing. This shock wave can be seen in the pressure distributions at BL 55 (Figure 8-18 (a)), BL 70 (Figure 8-18 (b)), BL 80 (Figure 8-18 (c)), and BL 95 (Figure 8-18 (d)). In the measurements however a pressure rise due to a shock wave is present at BL 55 (Figure 8-18 (a)) and at BL 95 (Figure 8-18 (d)) in a more downstream position. It is not present at the intermediate sections BL 70 and BL 80 (Figure 8-18 (b), Figure 8-18 (c)). At the outer wing sections (Figure 8-18 (e) and Figure 8-18 (f)) the measured pressure distributions are very different from the computed pressure distributions. The same effect was seen in a comparison of the results of the other participants of the AVT-113 task group ([8-19] and Chapter 16): all the numerical results, although obtained in different grids and by different codes (structured, unstructured) were very close but different to the measurements. These results and the fact, that the grid adaptation has shown no substantial effect on the results indicate that there is no grid effect on the disagreement between computed and measured results.

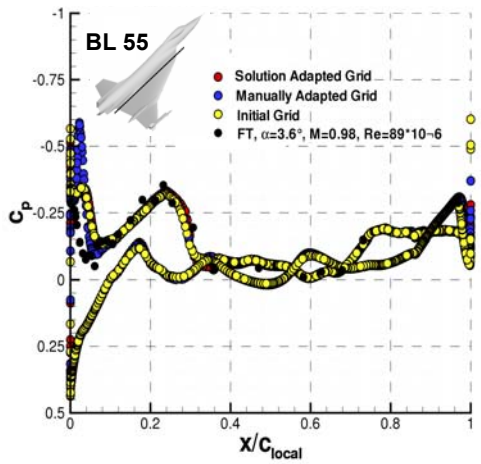

(a) BL 55

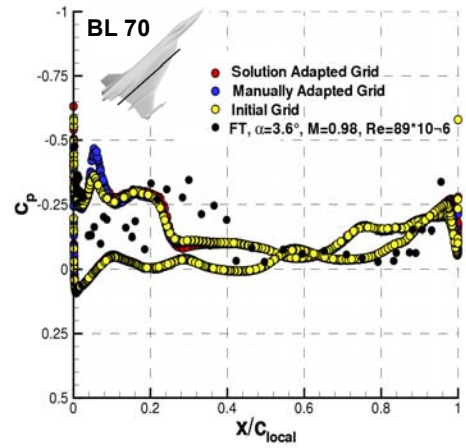

(b) BL 70

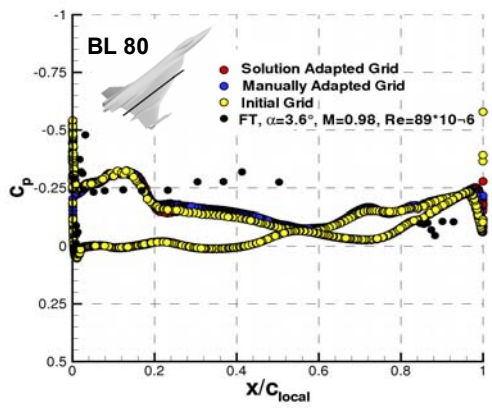

(c) BL 55

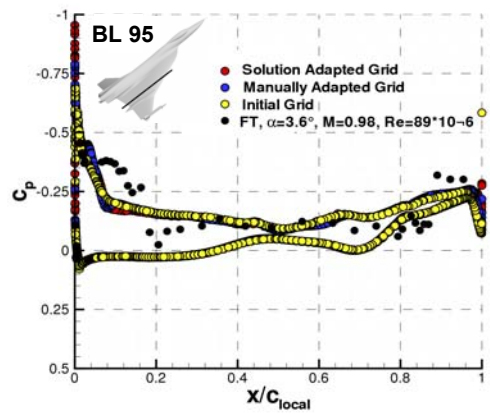

(d) BL 95

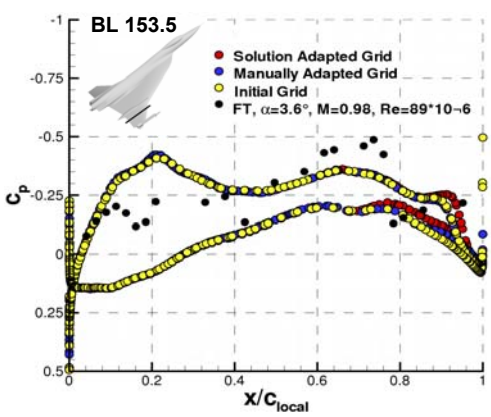

(e) BL153.5

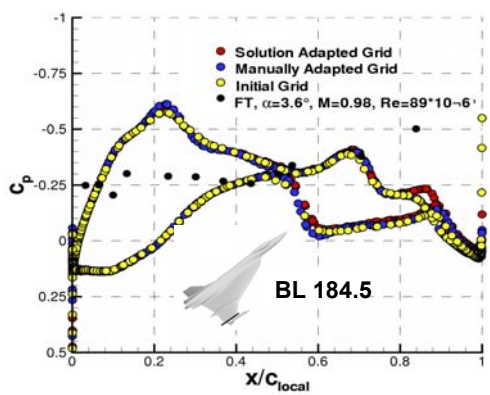

(e) BL184.5

Figure 8-18: Computed and Measured Surface Pressure Distributions at FC 70 (M_∞ = 0.97, α = 4.37°, Re = 88.77 x 10^6).

Figure 8-19 shows the y^+ distribution along the upper surface for FC 70. They are also in an acceptable range (values of $y^+ < 3$ are fine for the SAE turbulence model). So a defect of the grid resolution can be excluded. A defect of the flow solver can also be excluded, as all the different codes of the other participants show the same behavior for this flight condition (Ref. [8-19] and Chapter 16).

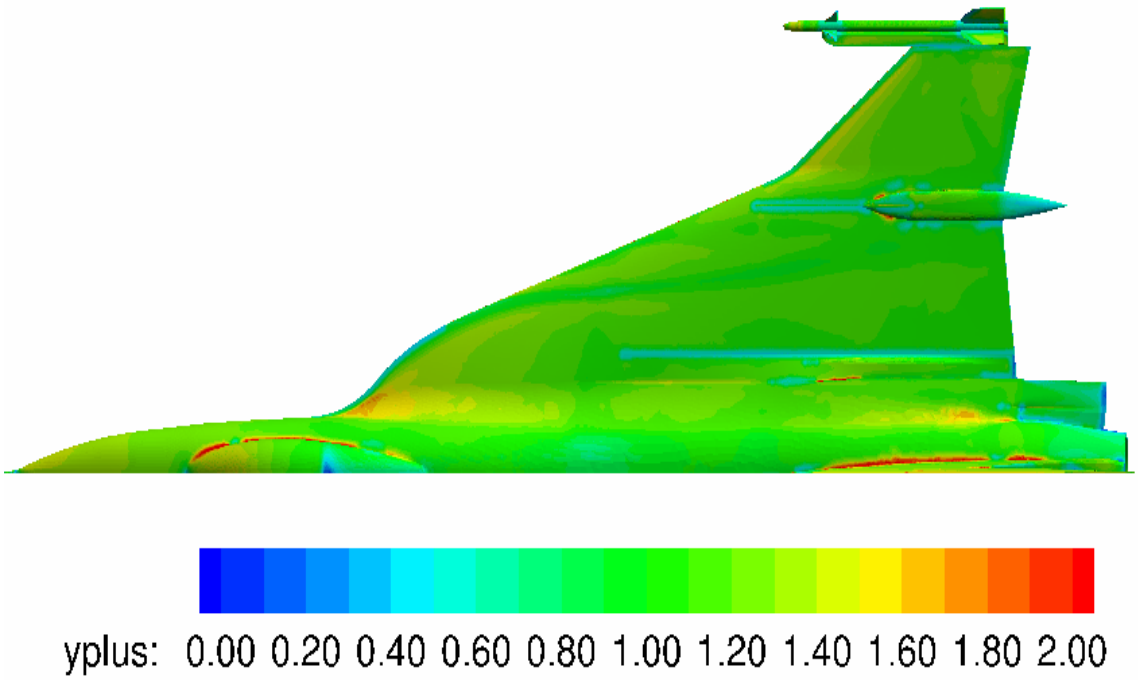

Figure 8-19: y^+ Distribution at Wing Upper Surface for FC 70 (M_∞ = 0.97, α = 4.37°, Re = 88.77 x 10^6).

8.8 CONCLUSIONS

With the framework of CAWAPI, it has been demonstrated, that flow field data measured on the F-16XL fighter aircraft can be predicted by CFD. The presented results underline, that all essential data like pressure distribution, velocity profiles, and skin friction coefficients can be predicted within a satisfactory accuracy (except for FC 70).The results also demonstrate, that that the solution based grid adaptation is a very powerful tool in order to get an optimum grid for a complex configuration and in order to fix grid dependencies in the solution.

But the static, sequential grid adaptation (computing the flow solution, adapting the grid, new pre-processing, new flow solution, etc.) as it was applied in the present study, is a very tedious task and requires some experience and several trial and error loops. For extensive numerical studies at complex configurations (e.g. computation of the aerodynamic control characteristics of a complete fighter aircraft) this kind of grid adaptation is not very suitable, as it requires a complicated solution- and grid bookkeeping and the necessary manual work leads to long turn-around times.

But in any case the solution based grid adaptation can help to generate an optimal pre-refined grid for a certain configuration, which then can be used for a wide range of flow conditions.

8.9 ACKNOWLEDGEMENTS

The author thanks all the members of the NATO RTO task group AVT-113 "Understanding and Modeling Vortical Flows to Improve the Technology Readiness Level for Military Aircraft" and particularly Dr. J.E. Lamar and Professor D. Hummel for their contributions during the course of this project.

8.10 REFERENCES

[8-1] Fournasier, L., Rieger, H., Tremel, U. and van der Weide, E.: *Time-Dependent Aeroelastic Simulation of Rapid Manouevring Aircraft*, AIAA Aerospace and Sciences Meeting and Exhibit, 2002, Reno, NV, CP949.

[8-2] Sørensen, K.A., Tremel, U., Rieger, H. and Hitzel, S.M.: *Simulation of Manoeuvring Fighter Aircraft with the Unstructured Chimera Approach*, AIAA-2007-0123, Presented at 45th AIAA Aerospace Sciences Meeting and Exhibit, Reno, NV, January 8-11, 2007.

[8-3] Lamar, J.E., Obara, C.J., Fisher, B.D. and Fisher, D.F.: *Flight, Wind-Tunnel and Computational Fluid Dynamics Comparison for Cranked Arrow Wing (F-16XL-I) at Subsonic and Transonic Speeds*, NASA TP-2001-210629, 2001.

[8-4] Lamar, J.E. and Obara, C.J.: *Review of Cranked-Arrow Wing Aerodynamics Project: Its International Aeronautical Community Role*, AIAA-2007-487, Presented at 45th AIAA Aerospace Sciences Meeting and Exhibit, Reno, NV, January 8-11, 2007.

[8-5] Boelens, O.J., Görtz, S., Morton, S., Fritz, W. and Lamar, J.E.: *Description of the F-16XL Geometry and Computational Grids Used in CAWAPI*, AIAA-2007-488, Presented at 45th AIAA Aerospace Sciences Meeting and Exhibit, Reno, NV, January 8-11, 2007.

[8-6] CentaurSoft Grid Generator, http://www.centaursoft.com (cited 10 June 2008).

[8-7] Gerhold, T., Friedrich, O., Evans, J. and Galle, M.: *Calculation of Complex Three-Dimensional Configurations Employing the DLR-TAU Code*, AIAA-97-0167, 1997.

[8-8] Schwamborn, D., Gerhold, T. and Kessler, R.: *The DLR-TAU Code – an Overview*, ONERA-DLR Aerospace Symposium, CP ODAS 99, 21-24 June 1999, Paris, France.

[8-9] Alrutz, T. and Rütten, M.: *Investigation of Vortex Breakdown over a Pitching Delta Wing Applying the DLR TAU-Code with Full, Automatic Grid Adaptation*, AIAA-2005-5162.

[8-10] Boelens, O.J., Spekreijse, S.P., Systma, H.A. and de Cock, K.M.J.: *Comparison of Measured and Simulated Flow Features for the Full-Scale F-16XL Aircraft*, AIAA Paper 2007-0489, Presented at 45th AIAA Aerospace Sciences Meeting and Exhibit, Reno, NV, January 8-11, 2007.

[8-11] Badcock, K.J.: *Evaluation of Results from a Reynolds Averaged Multiblock Code Against F-16XL Flight Data*, AIAA Paper 2007-0490, Presented at 45th AIAA Aerospace Sciences Meeting and Exhibit, Reno, NV, January 8-11, 2007.

[8-12] Elmiligue, A.A., Abdol-Hamid, K.S. and Massey, S.J.: *PAB3D Simulations for the CAWAPI F-16XL*, AIAA Paper 2007-0491, Presented at 45th AIAA Aerospace Sciences Meeting and Exhibit, Reno, NV, January 8-11, 2007.

[8-13] Morton, S.A., McDaniels, D.R. and Cumming, R.M.: *F-16XL Unsteady Simulations for the CAWAPI F-16XL Facet of RTO Task Group AVT-113*, AIAA Paper 2007-0493, Presented at 45th AIAA Aerospace Sciences Meeting and Exhibit, Reno, NV, January 8-11, 2007.

[8-14] Görtz, S. and Jirásek, A.: *Unstructured Steady/Unsteady Solutions with Edge for CAWAPI F-16XL at KTH/FOI*, AIAA Paper 2007-0678, Presented at 45th AIAA Aerospace Sciences Meeting and Exhibit, Reno, NV, January 8-11, 2007.

[8-15] Michal, T., Oser, M., Mani, M. and Ross, F.: *BCFD Unstructured-Grid Predictions on the F-16XL (CAWAPI) Aircraft*, AIAA Paper 2007-0679, Presented at 45th AIAA Aerospace Sciences Meeting and Exhibit, Reno, NV, January 8-11, 2007.

[8-16] Davis, M.B., Reed, C. and Yagle, P.: *Hybrid Grid Solutions on the (CAWAPI) F-16XL Using Falcon v4*, AIAA Paper 2007-0680, Presented at 45th AIAA Aerospace Sciences Meeting and Exhibit, Reno, NV, January 8-11, 2007.

[8-17] Karman, S., Michell, B. and Sawyer, S.: *Unstructured Grid Solutions of CAWAPI F-16XL by UT SimCenter*, AIAA Paper 2007-0681, Presented at 45th AIAA Aerospace Sciences Meeting and Exhibit, Reno, NV, January 8-11, 2007.

[8-18] Lamar, J.E. and Abdol-Hamid, K.S.: *USM3D Unstructured Grid Solutions for CAWAPI at NASA LaRC*, AIAA Paper 2007-0682, Presented at 45th AIAA Aerospace Sciences Meeting and Exhibit, Reno, NV, January 8-11, 2007.

[8-19] Rizzi, A., Badcock, K.J., Jirásek, A. and Boelens, O.J.: *What was Learned from Numerical Simulations of F-16XL (CAWAPI) at Flight Conditions*, AIAA Paper 2007-0683, Presented at 45th AIAA Aerospace Sciences Meeting and Exhibit, Reno, NV, January 8-11, 2007.